ELSEVIER

Contents lists available at ScienceDirect

# Journal of Manufacturing Processes

journal homepage: www.elsevier.com/locate/manpro





# Numerical investigation elucidating effects of microstructure on the transient thermomechanical phenomena during laser impact welding

Glenn Gleason, Sumair Sunny, Ritin Mathews, Arif Malik

The University of Texas at Dallas, Department of Mechanical Engineering, 800 W. Campbell Road, Richardson, TX 75080, USA

ARTICLE INFO

Keywords:
Laser impact welding
Eulerian framework
Microstructure
Inhomogeneity and anisotropy
Transient thermomechanical response

#### ABSTRACT

Transient thermomechanical phenomena such as extreme plastic strains and temperature spikes that occur during laser impact welding are impractical to experimentally observe given the sub-microsecond duration of the joining process. Thus, computational models are necessary to study in-situ behavior along the weld interface. While researchers have utilized computational models for such investigations, this work elucidates the specific influence of microstructure-level modeling that captures the associated inhomogeneity/anisotropic effects at smaller scales. An aluminum 1100-H19 flyer and a stainless steel 304-O target foil are modeled using an Eulerian framework to simulate cases with and without microstructure consideration during laser impact welding of dissimilar metallic foils. When considering microstructure modeling, variations in flow stress reveal intermittently elevated temperatures along the weld interface due to concentrations of shock pressure at relatively small grains; however, they are not found to be a significant source of instability initiating or influencing the joint formation. Grain refinement and material hardening are suggested within a 10 µm-thick zone of the flyer near the weld interface, while severe plastic deformation in the target indicates possible martensitic phase transformation. Grain boundary sliding driven by variations in yield surfaces among individual grains gives rise to relatively higher collision velocity. Consequently, higher plastic strain rates along with greater amounts of plastic heat dissipation at the interface result in increased material jetting at higher temperatures. Alternating transient shear stresses are predicted in each model, though the inhomogeneous model predicts the brief appearance of a concentrated shear zone in the rebound region which is not seen in the homogeneous model. This work illuminates correlations between microstructure and transient phenomena during laser impact welding of dissimilar metallic foils, thus demonstrating a numerical modeling approach extensible to numerous other impact welding processes that complete within a very short time span.

# 1. Introduction

Laser impact welding (LIW) is a technique for forming joints between solid surfaces, wherein a flyer is propelled at a high velocity towards a stationary target by confined, rapidly expanding plasma induced via pulsed laser irradiation, as illustrated in Fig. 1. This process resembles other impact welding methods in that there is no direct application of heat to form joints. LIW is notable for its utility at relatively smaller scales, however, allowing welds to be formed with greater precision and safety in certain applications. LIW has been successfully shown to join foils tens of micrometers thick of dissimilar metal alloys known to produce unfavorable weld characteristics in fusion processes [1,2], or between alloys that are infeasible to fusion weld due to mutual insolubility, even at high temperatures (e.g., magnesium and steel) [3]. Impact

techniques substantially increase the range of material combinations that may be joined, since fusion weldability is not of concern. This suggests their possible application in situations where designs must be considered according to other criteria, such as in microelectronics or biocompatible implants.

The use of laser-induced shock pressure to initiate the LIW process results in strain rates from  $10^6$  to  $10^7\,\mathrm{s}^{-1}$  in a foil flyer [4]. Additionally, the velocities at which the collision point travels in an impact welding interface is on the order of the speed of sound in the materials ( $\sim 0.2$  to  $1.5\,\mathrm{km}\,\mathrm{s}^{-1}$ ) [5]. Temperatures near at least one of the materials' melting points, severe plastic deformation, and high pressures occur in the narrow interfacial region, thus creating a weld absent intermetallic compounds [6]. Thin layers of oxides and other contaminants ablate from the surfaces in a jet of high-temperature particles, a phenomenon driven by extreme shear stresses near the collision point that oppose

E-mail address: arif.malik@utdallas.edu (A. Malik).

<sup>\*</sup> Corresponding author.

Nomenclature		t	Time
		$t_p$	Full-width half-maximum pulse width
Α	Johnson-Cook reference yield strength	$U_{i}$	Linear displacement ( $i = \{X, Y, Z\}$ )
a	Selective laser melting (SLM) parameter	$U_p$	Particle velocity
В	Johnson-Cook strain hardening coefficient	$\dot{U_s}$	Shock wave velocity
b	SLM parameter	v	Scan speed
C	Johnson-Cook strain rate hardening coefficient	$v_x$	Collision velocity
$c_0$	Bulk speed of sound	$\dot{\mathbf{X}}$	Velocity vector
$\mathbf{c}_{\mathbf{f}}$	SLM parameter	X	Position vector
$c_{r}$	SLM parameter	$\mathbf{x_i}$	Center of laser spot (X-direction)
$c_{\nu}$	Specific heat (constant volume)	$\alpha$	Energy ratio
$D_i$	Major diameter of grain i	Γ	Grüneisen material constant
$e_{\nu}$	Internal energy per unit volume	γ	Shock impedance (combined)
$e_m$	Internal energy per unit mass	γ <sub>Al</sub>	Shock impedance (aluminum)
$f_f$	SLM parameter	γg	Shock impedance (borosilicate glass)
$F_n$	Nodal forces	$\epsilon$	Emissivity
$f_r$	SLM parameter	$arepsilon_{ ext{eq}}$	Equivalent plastic strain
G	Elastic shear modulus	$\dot{\epsilon}_0$	Johnson-Cook reference strain rate
h	Convective heat transfer coefficient	$\epsilon_{el}$	Deviatoric elastic strain
$I_0$	Averaged laser pulse fluence	$\dot{arepsilon}_{ m p}$	Plastic strain rate
k	Thermal conductivity	$\dot{oldsymbol{arepsilon}_p}$	Plastic strain rate tensor
$k_y$	Strengthening coefficient	$\epsilon_p$	Plastic strain
L	Plasma layer thickness	$\eta^{r}$	Ratio of particle velocity to shock velocity
$L_e$	Finite element edge length	$\overset{\cdot}{ heta_{i}}$	Angular displacement ( $i = \{X, Y, Z\}$ )
m	Johnson-Cook thermal softening exponent	Λ	Absorptivity
n	Johnson-Cook strain hardening exponent	λ	Adiabatic constant
$n_l$	Number of node layers	ρ	Density
$\hat{n}$	Unit normal vector	σ	Stress tensor
P	SLM laser power	$\sigma_0$	Dislocation movement stress threshold
P	Laser-induced pressure	$\sigma_{ m d}$	Deviatoric stress
p	Shock wave pressure	$\sigma_{ m f}$	Flow stress
Q	Volumetric heat input	$\sigma_R$	Standard deviation of intensity distribution
R	Radial distance from spot center	$\sigma_{y, i}$	Yield strength of grain i
S	Ratio of $\Delta U_s$ to $\Delta U_p$	$ au_{ ext{XY}}$	In-plane (XY) shear stress
S	Source function (general)	ф	Solution variable (general)
T	Temperature	arphi	SLM surface designation
T*	Homologous temperature	Ψ	Flux function
$T_0$	Ambient temperature	Ψ	Stefan-Boltzmann constant
$T_{m}$	Melting temperature	,	

direction in the flyer and target [7]. Transient phenomena such as these resolve on very short timescales, making in-situ observation of the process challenging; this is particularly notable in the case of in LIW (vs. other larger-scale types of impact welding), which resolves within approximately 1  $\mu$ s due to the small dimensions of the parts being welded. Complex patterns of shear stress, severe plastic deformation, and thermal dissipation emerge in an unstable manner during collision, and experimental methods are limited in the information that may be captured before the process is complete. Therefore, many computational investigations utilizing physics-based finite element (FE) techniques

have been performed to try to explain the mechanisms that influence joint formation; a summary of recent works may be found in Table 1.

The continued application of computational methods to the problem of impact welding has yielded useful knowledge on the process. However, the effects of metallic microstructure when incorporated into numerical models have been minimally explored. Table 1 lists recent research that utilizes continuum-scale FE models, employing homogeneous material properties for the welded specimens. It is important to note that none of the previous studies have captured the effects of microstructure modeling. Given that previous works on impact welding

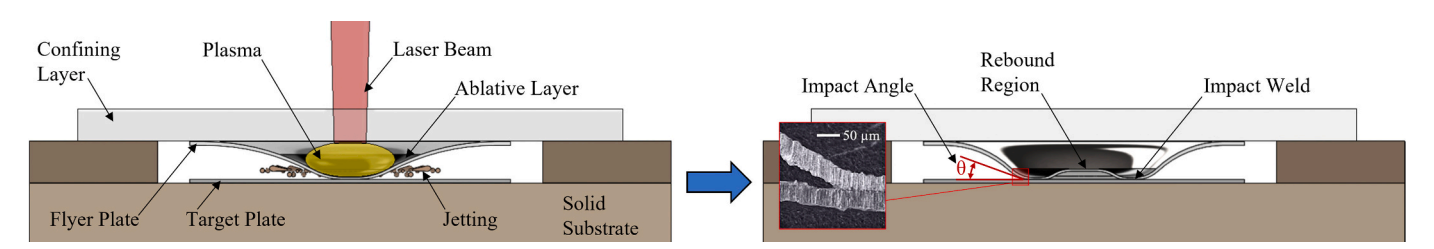


**Fig. 1.** (Left) Schematic of a laser impact welding process illustrating the expanding plasma that propels the flyer towards the stationary target. Upon impact, material jetting phenomena is observed. (Right) The resulting impact weld, featuring a rebound region that may develop [8]. (*Inset*) Optical micrograph featuring a cross section of an Al 1100 – SS 304 laser impact weld, adapted from an earlier publication by the authors [9].

Table 1
Summary of recent works pertaining to numerical modeling of transient phenomena in impact welding. Note, effects of grain structure were not captured

Author (year)	Process & materials (specification)	FE model formulation	Investigated quantities	Notable findings
Nassiri et al. (2017) [10]  Zhang et al. (2018)	Vaporizing foil actuator welding (VFAW); Ti-Cu (110) Explosive welding (EXW);	Arbitrary Lagrangian Eulerian (ALE), smoothed particle hydrodynamics (SPH)	Pressure Temperature Plastic strain Velocity (collision point) Temperature	<ul> <li>Simple wavy weld morphologies were successfully captured using ALE and SPH.</li> <li>Only SPH provided insights into waveforms with vortex shedding phenomena and jetting.</li> <li>Transient molten zones were predicted near vortices.</li> <li>Emergence of jet indentation mechanism predicted in EXW.</li> </ul>
[11]	Al (2024)-steel (4340)		<ul><li> Pressure</li><li> Weld interface</li><li> Jetting</li></ul>	<ul> <li>Qualitative similarities found between vortex shedding zones in model and experiment.</li> </ul>
Gupta et al. (2019) [12]	VFAW; Cu-Ti, Al (6061-T6)- Steel (4130)	Eulerian	<ul><li> Temperature</li><li> Velocity</li><li> Weld Interface</li></ul>	<ul> <li>Various impact velocities simulated to determine relationship between weld interface morphology and collision point velocity (compared to sound speeds in material).</li> </ul>
Gleason et al. (2020) [7]	LIW; Al (1100-H19)- stainless steel (304-O)	Eulerian	<ul><li> Temperature</li><li> Plastic strain</li><li> Velocity</li><li> Shear stress</li></ul>	<ul> <li>Impact angle found to increase with distance from spot center.</li> <li>Significant shear stresses found in flyer prior to impact.</li> <li>Transient alternating shear stresses due to elastic interactions found to trail the weld front.</li> </ul>
Lee et al. (2020) [13]	VFAW; Cu-Cu	SPH	<ul> <li>Pressure</li> <li>Temperature</li> <li>Plastic strain</li> <li>Velocity (collision point)</li> </ul>	<ul> <li>Rapid changes in plastic strain and temperature result in an impact affected zone at impact weld interface, distinct from the heat affected zones found in fusion welds.</li> <li>Molten zones must be brief and discontinuous to prevent brittle intermetallic formation.</li> </ul>
Liang et al. (2020) [14]	Underwater EXW, Al (1060)-BMG (Zr-based)	SPH	Plastic strain     Weld interface     Jet composition	<ul> <li>Simulation based on SPH framework predicted jetting of mostly Al composition preceding nearly flat weld interface formation.</li> <li>Johnson-Holmquist ceramics model applied to brittle BMG substrate.</li> <li>Plastic strain profiles of near-surface elements (particles) show severe plastic deformation of both materials, including the BMG.</li> </ul>
Meng et al. (2020) [15]	VFAW; Cu-Ti	SPH	<ul><li>Temperature</li><li>Velocity</li><li>Weld interface</li></ul>	<ul> <li>Modification of simulation parameters revealed a dependence of waveform dimensions on density ratio, impact velocity/ angle, and other parameters.</li> </ul>
Hosseinzadeh et al. (2021) [16]	Gas mixture detonation impact welding, Al (6061- T6)-Cu (OFHC)	Lagrangian	<ul><li>Plastic strain</li><li>Velocity</li><li>Stress (von Mises, shear)</li></ul>	<ul> <li>Shear stress temporal profile at traveling collision point used to confirm weld formation time.</li> <li>Equivalent plastic strain thresholds used to predict geometry of welds.</li> </ul>
Li et al. (2021) [17]	Magnetic pulse welding (MPW); Al (6060-T6)-Cu	Eulerian (for interface mechanics)	<ul><li> Temperature</li><li> Plastic strain</li><li> Velocity</li><li> Weld interface</li></ul>	<ul> <li>Wavy interface morphology is shown to form via repeated deformations of flyer and target surfaces during weld, not in a simultaneous surface distortion.</li> <li>Localized high-temperature zones predicted by FE model in good agreement with intermetallic compound zones found in experiment.</li> </ul>
Li et al. (2021) [18]	LIW; Ti (TA1)-Ni	Coupled SPH-Lagrangian, SPH, Eulerian	<ul><li> Plastic strain</li><li> Velocity</li><li> Shear stress</li></ul>	<ul> <li>High jet temperature predictions partly caused by isolation of ablated material from substrate.</li> <li>Tracking thermal history of individual nodes allows characterization of weld interface due to transient temperature effects.</li> </ul>
Lu et al. (2021) [19]	LIW; Ti (TA1)-brass (H62)	SPH	Pressure     Temperature     Plastic strain     Shear stress     LIW cross-sectional     morphology	<ul> <li>Transient oscillations in jet ejection direction modeled in SPH used to show transition in weld interface morphology at increasing values of laser energy used for welding.</li> <li>Jet indentation mechanism shown to include participation from both specimens' materials, as opposed to only the lower-density material (Ti flyer) considered in other analyses [1,20].</li> </ul>
Xiong et al. (2021) [3]	VFAW; Mg (AZ31)-steel (DP590)	Eulerian (impact phase), Meshed Lagrangian (cooling phase)	Pressure     Temperature	<ul> <li>Conditions at impact weld analyzed via FE model to explain porosity and cracks at interlayer between Mg-Steel interface.</li> <li>Fe found to be diffused/mixed into a deposit layer formed by local melting of Mg, contributing to a metallurgical bond without a wavy interface/interlocking.</li> </ul>
Gleason et al. (2022) [21]	LIW; Al (1100-H19)- Stainless steel (304-O)	Eulerian	<ul><li> Velocity</li><li> Temperature</li><li> Plastic strain</li></ul>	<ul> <li>Extreme shock pressures concentrate at small, hard grains of SS 304, resulting in local thermal spikes at weld</li> <li>Equivalent plastic strains crossing an exothermic phase transformation range are achieved in the SS 304 target during weld</li> </ul>

have noted the role of dynamic instability in the initiation and development of impact weld interfaces [22], this work seeks to provide further novel insights into the effects an inhomogeneous grain structure may have as the joining process proceeds. Variations in grain structures are known to arise for fabrications by additive manufacturing (AM) (e. g., selective laser melting (SLM)), resulting in inhomogeneity and anisotropy in the material properties, and thus presents challenges in

predicting the response of parts during subsequent processing. Indeed, continued investigations of the corresponding inhomogeneous thermomechanical behavior in such parts present opportunities to tailor AM microstructures to realize improved LIW strength.

First, a prediction of the inhomogeneous grain structures for AM aluminum and stainless steel foils are established via a Dynamic Kinetic Monte Carlo (KMC) model, described further in Section 2.1. Section 2.2

outlines the Eulerian numerical formulation used for the FE model. Following this, Section 2.3 details the model layout and boundary conditions, while Section 2.4 describes the material modeling. A discussion of the results from the inhomogeneous material model is provided in Section 3, with comparisons made to a homogeneous LIW model to better elucidate the importance of microstructure modeling on prediction of transient phenomena. Finally, key findings and concluding remarks are summarized in Section 4.

## 2. Numerical modeling

To obtain a 3D microstructure model that can be implemented in the numerical framework for each foil, the foils are considered to be AM via SLM, as discussed by [23]. This process would give rise to variations in microstructure, i.e., a mix of columnar (or elongated) grains that grow towards the direction of maximum thermal gradient, and finer, equiaxed grains that form along the path of the scan lines. Such variations are hypothesized to influence the transient, anisotropic thermomechanical responses during LIW. In this section, the SLM model is first discussed, from which the thermal history is used as input for a Dynamic KMC simulation [24] for grain structure prediction. The predicted microstructure is subsequently spatially mapped into an Eulerian grid, wherein an LIW experiment by the authors [9] is emulated. The influence of variation in grain size during the highly dynamic process, for both the flyer and target foils, is captured by implementing a Johnson-Cook Hall-Petch (J-C H-P) material model [27], along with a linearized Hugoniot Equation of State [28].

#### 2.1. Selective laser melting model

An SLM numerical model to predict the thermal history is depicted in Fig. 2. A 4 mm  $\times$  5 mm patch on the top surface of a 50  $\mu$ m thick layer of powder, atop a 25.4 mm square  $\times$  3.2 mm deep substrate is scanned in a raster pattern as illustrated. The thermal history of the process is governed by Eq. (1) which represents the 3D heat conduction in the model. Temperature-dependent material parameters such as thermal conductivity, k, specific heat (constant volume),  $c_v$ , and density,  $\rho$ , are adopted from literature for both metals [29,30]. The transient, volumetric heat energy input, Q, is modeled using a double ellipsoid Gaussian heat source described by Eq. (2), introduced by Goldak et al. [26], which captures the influence of scan speed, v, laser power, v, and absorptivity, v, v. The heat input process parameters adopted in this work, for both the aluminum 1100-H19 (Al 1100) flyer and stainless steel 304-O (SS 304) target, are summarized in Table 2.

$$\nabla \bullet (k\nabla T) + Q = c_{\nu}\rho \frac{\partial T}{\partial t}, \quad \text{for } t \ge 0$$
 (1)

**Table 2** SLM process parameters and calibration constants [23,34–36].

Parameter	Al 1100	SS 304
SLM process model		
P (W)	175	200
v (m s <sup>-1</sup> )	0.195	0.8
Scan pattern	Raster	Raster
Layer thickness (µm)	50	50
Hatch spacing (µm)	50	50
Λ	0.35	0.4
$\epsilon$	0.32	0.56
$h \text{ (W m}^{-2} \text{ K}^{-1})$	10	10
Heat source model		
a (μm)	160	180
b (μm)	160	180
c <sub>f</sub> (μm)	276	180
c <sub>r</sub> (µm)	1520	540
$ m f_{f}$	1.4	1.4
$f_r$	0.6	0.6

$$Q = \begin{cases} \frac{6\sqrt{3} \, f_f P \Lambda}{a b c_f \pi \sqrt{\pi}} e^{-3\frac{Z^2}{a^2}} \, e^{-3\frac{Y^2}{b^2}} \, e^{-3\frac{(X+vt)^2}{c_f^2}}, X \ge x_i \\ \frac{6\sqrt{3} \, f_r P \Lambda}{a b c_r \pi \sqrt{\pi}} e^{-3\frac{Z^2}{a^2}} \, e^{-3\frac{Y^2}{b^2}} \, e^{-3\frac{(X+vt)^2}{c_f^2}}, X < x_i \end{cases}$$
 (2)

A *DFLUX* user subroutine is scripted herein to continually update the position of the scanning laser and is recomputed during every increment of the thermal solution. Eq. (2) represents a piecewise-continuous function moving linearly along the X direction. For all  $X \geq x_i$ , the frontal heat distribution fraction is computed, and for all  $X < x_i$ , the aft heat distribution fraction is computed. Calibration constants for the heat source model are provided in Table 2 and details regarding calibration of the heat input model can be referenced from [24].

Since pre-heating of the substrate is not considered in this work, as an initial condition, the entire model is set to ambient temperature,  $T_0$ , as given by Eq. (3).

$$T(\mathbf{X},0) = T_0 \tag{3}$$

As heat is added, during scans, internal heat transfer via conduction, convection and radiation on surface  $\varphi$  is modeled per Eq. (4), which describes the surface energy balance of the system. In Eq. (4),  $\epsilon$  is the emissivity, h is the convective heat transfer coefficient, and  $\psi$  is the Stefan-Boltzmann constant (5.6704  $\times$  10<sup>-8</sup> W m<sup>-2</sup> K<sup>-4</sup>).

$$-k\nabla \mathbf{T} \bullet \hat{\mathbf{n}} + h(\mathbf{T} - \mathbf{T}_0) + \psi \epsilon (\mathbf{T}^4 - \mathbf{T}_0^4) = 0 \text{ on surface } \varphi$$
 (4)

The thermal history, once predicted, is used as input for the Dynamic

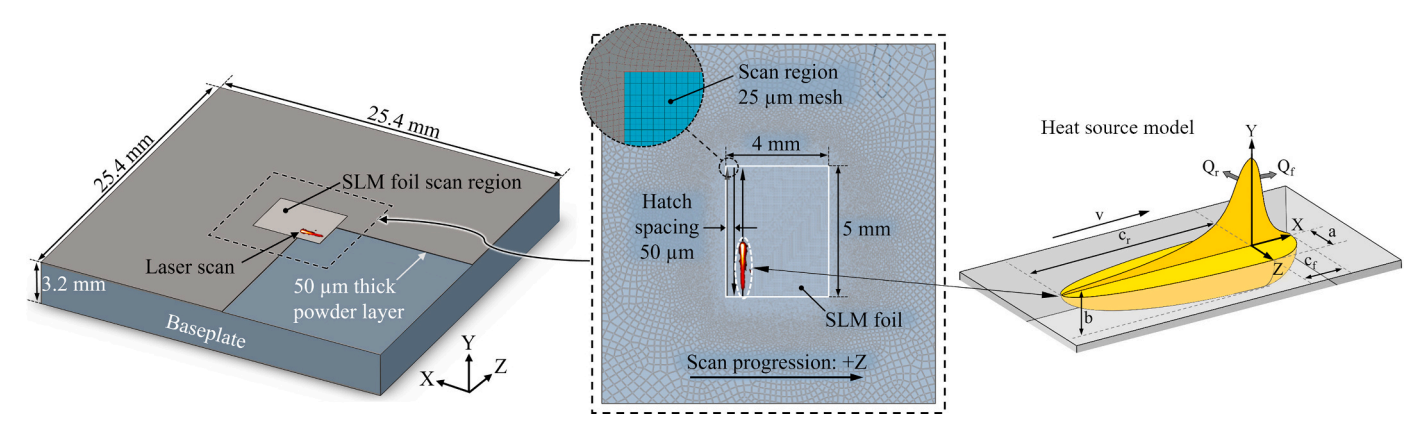


Fig. 2. (*Left*) Schematic of the SLM model to manufacture metal foils (having inhomogeneous microstructure). All dimensions are adapted from thermography experiments conducted by NIST [25]. A geometrically identical model is used for Al 1100 and SS 304, with only the temperature-dependent material properties, SLM & heat source parameters, and thermal calibration differing. (*Right*) Double ellipsoid heat source model [26] used to model the scanning laser.

KMC. The advantage of the Dynamic KMC over the conventional KMC technique [31] is that it captures the influences of intra- and interlayer heat accumulation on grain growth and nucleation prediction. After calibration the method can predict grains in FCC and BCC structures. Given that both metals used herein, for the flyer and target foils, have FCC crystal structures [32,33], the Dynamic KMC approach is applicable. An advantage of 3D microstructure prediction over electron backscatter diffraction (EBSD) imaging is that the experimental approach only offers 2D data and suitable assumptions must be made for out-of-plane grain dimensions. This can introduce errors in the framework. Nevertheless, EBSD imaging has been used to help verify the model calibration; for details on the Dynamic KMC framework and its calibration the reader is referred to [24].

The microstructure, once predicted, is mapped as a volume fraction into an Eulerian grid, discussed next, via a Python script. Each grain being mapped will accordingly also have its very own material definition, based on the respective grain's major diameter,  $D_i$ , obtained using a spherical fit to circumscribe the grain.

# 2.2. Eulerian numerical formulation

Eulerian models are useful for modeling fluid transport and severe solid deformation problems, thus making them appropriate for LIW considering the extreme strain (>20%) and strain rates involved in the laser-based manufacturing process. The Eulerian approach uses a spatially fixed mesh that is entirely remapped during every solution increment, avoiding mesh distortion errors that would occur in the case of a Lagrangian approach. Additionally, in contrast to a smoothed particle hydrodynamics framework, the Eulerian frame allows the laser-induced plasma pressure load described in the next subsection to be applied to the flyer.

The governing Eqs. (5)–(7) describe conservation of mass, momentum, and energy within the Eulerian domain, respectively. In Eqs. (5)–(7),  $\dot{\mathbf{X}}$ ,  $\boldsymbol{\sigma}$ ,  $\dot{\boldsymbol{\varepsilon}}_p$ , t, and  $e_v$ , represent the velocity vector, stress tensor, plastic strain rate tensor, time, and internal energy per unit volume, respectively.

$$\frac{\partial \rho}{\partial t} + \nabla \cdot \left( \rho \dot{\mathbf{X}} \right) = 0 \tag{5}$$

$$\frac{\partial \rho \dot{\mathbf{X}}}{\partial t} + \nabla \cdot \left( \rho \dot{\mathbf{X}} \otimes \dot{\mathbf{X}} \right) = \nabla \cdot \mathbf{\sigma} \tag{6}$$

$$\frac{\partial e_{v}}{\partial t} + \nabla \cdot \left( e_{v} \dot{\mathbf{X}} \right) = \mathbf{\sigma} : \dot{\mathbf{\varepsilon}}_{p} \tag{7}$$

Eq. (8) represents the generalized form of Eqs. (5)–(7), where  $\Psi$  is a flux function, S is a source function, X is the position vector, and  $\varphi$  is a solution variable.

$$\frac{\partial \phi}{\partial t} + \nabla \cdot \Psi \Big( \phi, \dot{\mathbf{X}}, \mathbf{X}, t \Big) = \mathbf{S} \tag{8}$$

Eqs. (9) and (10) are obtained via operator splitting in Eq. (8) and are solved in separate steps during each Eulerian solution increment.

$$\frac{\partial \phi}{\partial t} = S \tag{9}$$

$$\frac{\partial \phi}{\partial t} + \nabla \cdot \Psi \Big( \phi, \dot{\mathbf{X}}, \mathbf{X}, t \Big) = \mathbf{0}$$
 (10)

Eq. (9) takes the form of a Lagrangian governing equation with the only exception being the terms on the left side where a material time derivative is used in place of the spatial time derivative. To avoid displacement across more than one element length, solution variables are calculated within a sufficiently small time increment on a temporary Lagrangian mesh. This Lagrangian mesh is then remapped to the stationary Eulerian grid and the solutions to Eq. (10) account for changes in solution variables on the fixed mesh due to advection. This process

allows for equivalent plastic strain, internal energy, and mass to be tracked throughout the LIW process.

#### 2.3. Laser impact welding process model

An LIW experiment documented in previous work by the authors is emulated by the model illustrated in Fig. 3; the general approach used, except without microstructure, has shown good overall agreement with experimental observation [9]. The thermomechanical model assumes a plastic heat dissipation fraction,  $\sigma : \dot{\epsilon}_p$  (ref. Eq. (7)) of 90%. The FE model features a linear hexahedral Eulerian mesh having thermal and translational degrees of freedom. The cubic elements have an edge length,  $L_e$ , of 2 µm and hence reduced integration is implemented to decrease computational time. The transparent borosilicate glass overlay and stainless steel substrate are modeled as Lagrangian discrete rigid bodies; they are not involved in the weld formation which occurs entirely within the Eulerian domain. Both rigid bodies are constrained in translation ( $U_X = U_Y = U_Z = 0$ ) to emulate the experiment conditions. The 50  $\mu m$  thick Al 1100 flyer foil and SS 304 target foil are both modeled within the Eulerian domain and are separated only by a 260  $\mu m$ standoff distance that has been experimentally found to offer successful welds.

As described earlier, for both flyer and target, the predicted volume fractions with corresponding material assignments comprise the entire foil volume being modeled. As a simplification, the standoff region is treated as a void, i.e., no material (e.g., gas medium) assignment. Since the transient phenomena should manifest radially outward from the laser shot center, a symmetry condition ( $U_X = \theta_Y = \theta_Z = 0$ ) is applied on plane X = 0 to further reduce the computational cost and the out-ofplane thickness is limited to 6 µm. Since the out-of-plane characteristics are not being studied, a displacement boundary condition ( $U_Z = 0$ ) restricting motion along the Z direction is imposed throughout. This enforces a simplifying plane strain condition, validated by experimental observations by Lee et al., who noted less impact weld morphology variation in the direction normal to the weld cross section [37]. Furthermore, based on experimental observation since the annulus of the weld does not exceed 600 µm, the radial length (X direction) of the modeled foils is limited to 600 μm. A no-slip, isotropic Coulomb friction condition is implemented to capture the shear interaction between the colliding foil surfaces. Correspondingly, the coefficient of dry friction is estimated to be 0.6 [38]. This is found to be appropriate as per observations by Raoelison et al. [39], wherein impact welds were formed without slip or debonding.

A spatial and temporally varying laser-driven plasma pressure pulse is modeled based on experimental characterization documented by Hatamleh et al. [40]. Fabbro et al.'s 1D hydrodynamic model is used to develop a piece-wise continuous plasma pressure temporal profile given by Eq. (11) [41]. As depicted in Fig. 3, there is a heating phase,  $t < t_p$ , followed by an adiabatic cooling phase,  $t \ge t_p$ , at the confined ablation interface.

$$P(t) = \begin{cases} \frac{1}{10} \left\{ \left[ \frac{\alpha \gamma I_0}{2\alpha + 3} \right] \left[ 1 - \left( \frac{L(0)}{L(t)} \right)^2 \right] \right\}^{\frac{1}{2}}, \text{ for } t < t_p \\ P(t_p) \left[ \frac{L(t_p)}{L(t)} \right]^{\lambda}, \text{ for } t \ge t_p \end{cases}$$

$$(11)$$

The initial plasma thickness L(0), is estimated to be 10  $\mu$ m and the combined shock impedance,  $\gamma$ , at the confined ablation interface is calculated by Eq. (12), where  $\gamma_{Al}$  and  $\gamma_g$  represent the aluminum foil and borosilicate glass impedances, respectively.

$$\gamma = \frac{\gamma_{Al}\gamma_g}{2(\gamma_{Al} + \gamma_g)} \tag{12}$$

A peak pressure of 2.7 GPa, calculated at time  $t_p$  during the LIW simulation, is used to scale a normalized spatial pressure profile. This

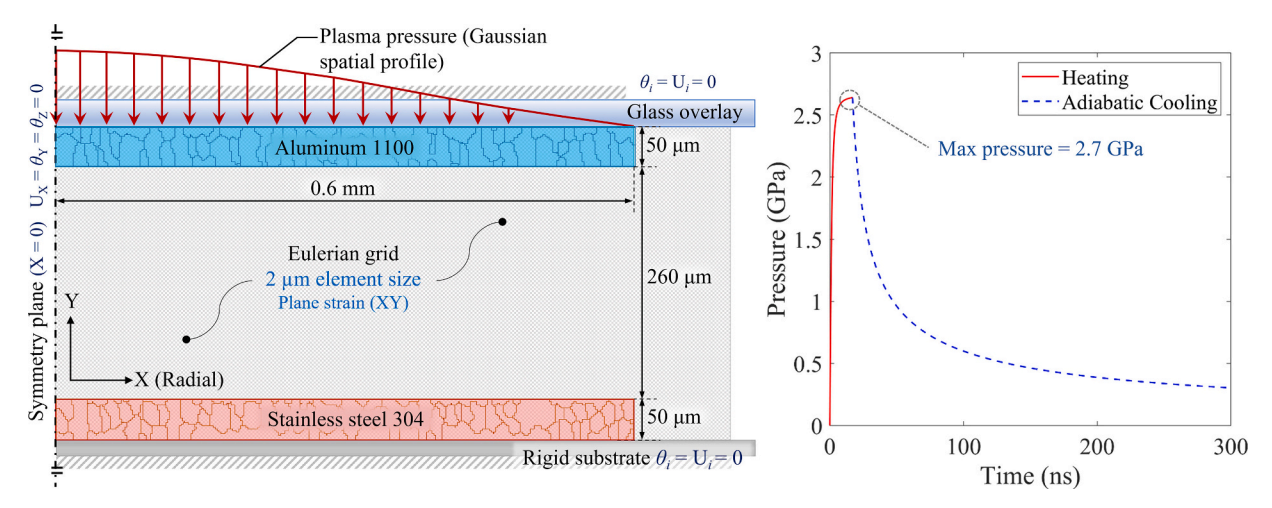


Fig. 3. (Left) A schematic of the laser impact welding process model used to emulate experiments documented in [9], showing the Gaussian spatial plasma pressure profile used to replicate realistic loading conditions. (Right) Experimentally characterized plasma pressure temporal profile.

profile is obtained from experimentally acquired spatial laser pulse intensity data in the form a 3D point cloud [40]. The 3D point cloud is scaled from pixels to radial distance, R, from the spot center (X=0), and undulating noise is filtered before a Gaussian profile, P(R), described by Eq. (13), is fit to the data. This simplification facilitates modeling of the load in the Eulerian plane strain configuration and provides to the flyer foil a more realistic velocity profile and deformed shape prior to impact [7]. In Eq. (13), the standard deviation,  $\sigma_R$ , describes the dispersion of the 3D point cloud data from the laser spot center. The peak plasma pressure,  $P(t_p)$ , (ref. Eq. (11)), obtained from the 1D hydrodynamic model, is used to scale the normalized spatial pressure distribution. A summary of the hydrodynamic model parameters used to compute the peak pressure temporal pressure profile are given in Table 3.

$$P(R) = \frac{1}{\sigma_R \sqrt{2\pi}} e^{-\frac{1}{2} \left(\frac{R}{\sigma_R}\right)^2} R \ge 0$$
(13)

The Gaussian plasma pressure profile, P(R), is represented by an equivalent distribution of concentrated nodal forces,  $F_n(R)$ , apportioned equally among all the nodes,  $n_l$ , that span the 50  $\mu$ m thick flyer (Y direction), as described by Eq. (14). During the confined ablation induced loading phase a peak nodal force magnitude of  $3.24 \times 10^{-4}$  N is predicted.

$$F_n(R) = \frac{L_e^2 P(R)}{n_l} \tag{14}$$

# 2.4. Material model for laser impact welding

Since the Dynamic KMC method used to predict the 3D microstructure does not provide information about crystal lattice orientation, approaches such as crystal plasticity finite element techniques cannot be implemented. A more rudimentary approach is adopted herein, where the Hall Petch (H-P) relation given by Eq. (15), is used as the yield strength parameter in the Johnson Cook (J-C) plasticity model given by

**Table 3**1D hydrodynamic model parameters [40–42].

Hydrodynamic model parameter	Value	
FWHM pulse width, $t_p$	~17 ns	
Averaged laser pulse fluence, $I_0$	$1.8~\mathrm{GW~cm^{-2}}$	
Energy ratio, $\alpha$	0.25	
Adiabatic constant, $\lambda$	1.4	
Glass shock impedance, $\gamma_g$	$1.14 \times 10^6 \ \mathrm{g \ cm^{-2} \ s^{-1}}$	
Al shock impedance, $\gamma_{Al}$	$2.75  imes 10^6 \ g \ cm^{-2} \ s^{-1}$	

Eq. (16) [43–45]. Individual grains are assigned unique yield strengths,  $\sigma_{y, i}$ , per Eq. (15), calculated based on their individual major diameters,  $D_i$ , which can be rationalized given that the major diameter of nonspherical grains corresponds to the lowest strength direction in a polycrystalline alloy [46]. In Eq. (15),  $\sigma_0$  is the threshold stress beyond which dislocations will move, and  $k_v$  is the strengthening coefficient.

$$\sigma_{y,i} = \sigma_0 + \frac{k_y}{\sqrt{D_i}} \tag{15}$$

In conjunction with grain size dependency, a strain-rate dependent and temperature dependent J-C plasticity model, per Eqs. (16)–(17), is implemented for its ability to capture the dynamic responses that occur during the high strain rates and elevated temperatures from plastic heat dissipation experienced in LIW [47].

$$\sigma_{\rm f} = \left[ A + B \left( \varepsilon_p \right)^n \right] \left[ 1 + C \ln \left( \frac{\dot{\varepsilon}_p}{\dot{\varepsilon}_0} \right) \right] \left[ 1 - (T^*)^m \right] \tag{16}$$

$$T^* = \begin{cases} 0 & \text{for } T < T_0 \\ \left(\frac{T - T_0}{T_m - T_0}\right) & \text{for } T_0 \le T \le T_m \\ & \text{for } T > T_m \end{cases}$$
 (17)

As the laser induced shock waves propagate through the surface of the metal, a small increase in entropy occurs given the large bulk moduli and adiabatic index at ambient conditions [48]. The Mie-Grüneisen equation of state, given by Eqs. (18)–(19), describes the resulting volumetric stress-strain response, associated to changes in pressure, p, and volume, during the LIW process. The presented model implements a Hugoniot form featuring a linearized relation between shock wave velocity  $U_s$  and particle velocity  $U_p$ , where  $c_0$  is the bulk speed of sound within the dissimilar foil materials,  $\eta$  is the ratio of  $U_p$  to  $U_s$ , s is the ratio of change in  $U_s$  to change in  $U_p$ ,  $e_m$  is the internal energy per unit mass, and  $\Gamma$  is a dimensionless Grüneisen parameter capturing thermodynamic material response.

$$p = \frac{\eta \rho c_0^2}{(1 - s\eta)^2} \left( 1 - \frac{\eta \Gamma}{2} \right) + \Gamma \rho e_m$$
 (18)

$$U_s = c_0 + sU_p \tag{19}$$

Additionally, Eq. (20) captures the deviatoric stress-strain response of each foil, where  $\sigma_d$  is the deviatoric stress, G is the elastic shear modulus, and  $\epsilon_{el}$  is the deviatoric elastic strain. All the LIW material constitutive model parameters are given in Table 4.

**Table 4**Laser impact welding material model parameters [1,20,28,49-51].

Parameters	Al 1100	SS 304		
Hall-Petch parameters				
$\sigma_0$ (MPa)	9.7	147.4		
$k_y$ (MPa $\mu m^{-0.5}$ )	41	551.67		
Johnson-Cook plasticity				
A (MPa) ref. Eq. (15)	$\sigma_{v, i}$	$\sigma_{v, i}$		
B (MPa)	345.5	1500		
C	0.001	0.014		
$\dot{\varepsilon}_0$ (s <sup>-1</sup> )	1	1		
n	0.183	0.36		
m	0.895	1		
$T_0$ (K)	293	293		
$T_{m}(K)$	916	1673		
Equation of state				
$\rho \text{ (kg m}^{-3}\text{)}$	2712	7905		
$c_0  (\text{m s}^{-1})$	5451.8	4722		
s	1.2592	1.441		
Γ	2.14	1.93		
G (GPa)	27.4	78		

$$\sigma_{\rm d} = 2G\varepsilon_{el} \tag{20}$$

By modeling individual grains as unique volume fractions and assigning to them distinct plasticity behavior, the foils can be considered as having inhomogeneous microstructures. As mentioned earlier, to illuminate the anisotropic effects on transient phenomena such as shear stress and temperature spikes associated to the distribution of plastic strain during impact as a result of the inhomogeneous model, an identical simulation is executed featuring homogeneous Al 1100 flyer and homogeneous SS 304 target. All material parameters listed in Table 4 are applied, however the J-C yield strength remains constant throughout the volume of the foils, i.e., 148.4 MPa and 110 MPa, respectively, for the Al 1100 flyer and SS 304 target [1]. Results of the LIW simulation, which

focus on transient interfacial material behavior when comparing the inhomogeneous and homogeneous models, are discussed next.

#### 3. Results and discussion

To study the changes in the transient phenomena during the impact weld formation, three sub-microsecond time frames, at 475, 575, and 675 ns, respectively, are examined, as depicted in Fig. 4. Additionally, Fig. 4 includes a 400 ns frame, to reveal the shape of the grains in both foils just prior to impact. As the weld forms, observations radially outward from the weld center (X = 0 mm) show that the impact angle increases and grains become more elongated; this agrees with experimental observations where more elongated grains suggest a greater degree of dynamic shear strain and the likelihood of adiabatic shear bands (ASB) [52]. ASB results when thermal softening in the material reaches a point beyond which strain hardening is no longer possible, such that any plastic heat dissipation causes an adiabatic rise in temperature, thereby inducing plastic flow instability [53]. The presence of ASB indicates work hardening given that the high shear deformation can increase dislocation density [54]. ASB is often observed alongside dynamic recrystallization (DRX) [55], however it should be noted that prediction of DRX is a limitation of the implemented Dynamic KMC microstructure prediction tool. As seen in Fig. 4, the aluminum grains (blue) reveal relatively more elongation in comparison to the stainless-steel grains (red). Since H-P strengthening is implemented in the material constitutive modeling, AM process-parameter dependent grain sizes have direct influence the range of yield strength, as depicted by the colormap. Considering the high strain rates associated with LIW, differences in the stacking fault energy (SFE) for both metals influence the choice of H-P coefficients [56]. Furthermore, the alloy composition for steel will also influence the choice of H-P coefficients, given its low SFE. Beyond changes in impact angle, differences in yield strengths, SFE for the two dissimilar metals, and differences in velocity during collision, the effect of grain-boundary sliding (GBS), i.e., shear movement at the boundary shared among neighboring grains, should also be noted.

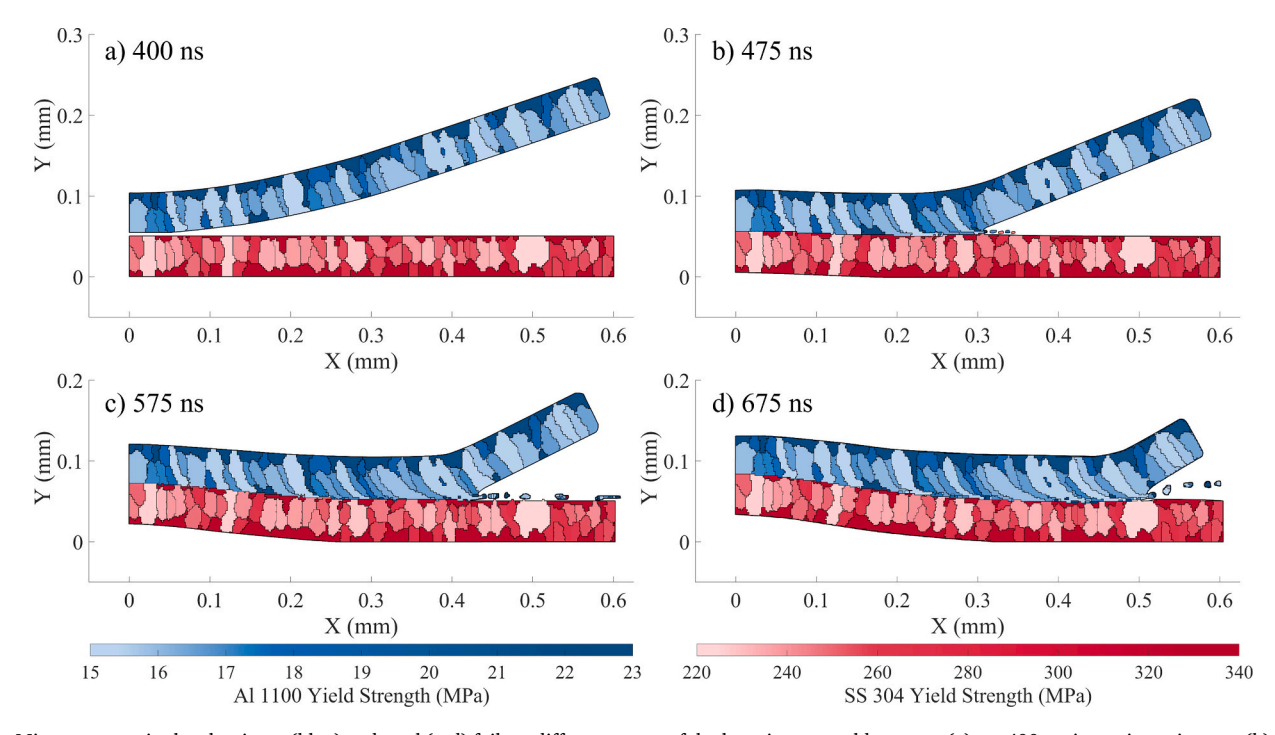


**Fig. 4.** Microstructure in the aluminum (blue) and steel (red) foils at different stages of the laser impact weld process: (a) t = 400 ns, just prior to impact, (b) t = 475 ns, just after formation of the impact weld, (c) t = 575 ns, during weld formation, increased jetting and an increasing impact angle, and finally (d) t = 675 ns, towards the end of weld formation, when aluminum grains near the mouth of the weld show the greatest elongation. (For interpretation of the references to color in this figure legend, the reader is referred to the web version of this article.)

GBS is more prominent when deformation occurs at temperatures exceeding 45% of the respective metal's melting point.

Weld formation between the two colliding dissimilar foils does not occur at the moment of initial contact, t=425 ns, but is confirmed once the initial jetting of material seen at t=475 ns, as shown in Fig. 5 (top). During the initial few nanoseconds of interfacial contact, the relatively small impact angle inhibits initiation of the shear instability necessary to ablate the colliding foil surfaces under high pressure and bring them into interatomic-scale contact. Between t=450 ns to 475 ns,  $v_x$  peaks at  $\sim 4050$  m s<sup>-1</sup> and 3850 m s<sup>-1</sup> for the homogeneous and inhomogeneous models, respectively. Around t=475 ns, reflected pressure waves cause internal spallation and rebound, as was experimentally observed by [1]. A build-up of compressive stress predicted between the target and the

rigid substrate drives a transient rise in temperature at the bottom of the target. Note, this is effect is only prominent in the inhomogeneous model and not the homogeneous one. By this stage of the LIW process, both models already exhibit subtle differences in peak equivalent plastic strain,  $\varepsilon_{\rm eq}$ , and distribution of temperature, T, along the weld interface as seen in Fig. 5 (top left). Moreover, the localized peaks do not overlap between the models, illuminating the effect that inclusion of microstructure modeling has in the numerical framework.

At t = 575 ns (ref. Fig. 5 *middle*), both models exhibit jetting, which reveals that the respective welds are underway, albeit the inhomogeneous model predicts a greater volume of ejecta as compared to the homogeneous model. Other noteworthy observations when comparing the inhomogeneous model with the homogeneous one include: (1) GBS

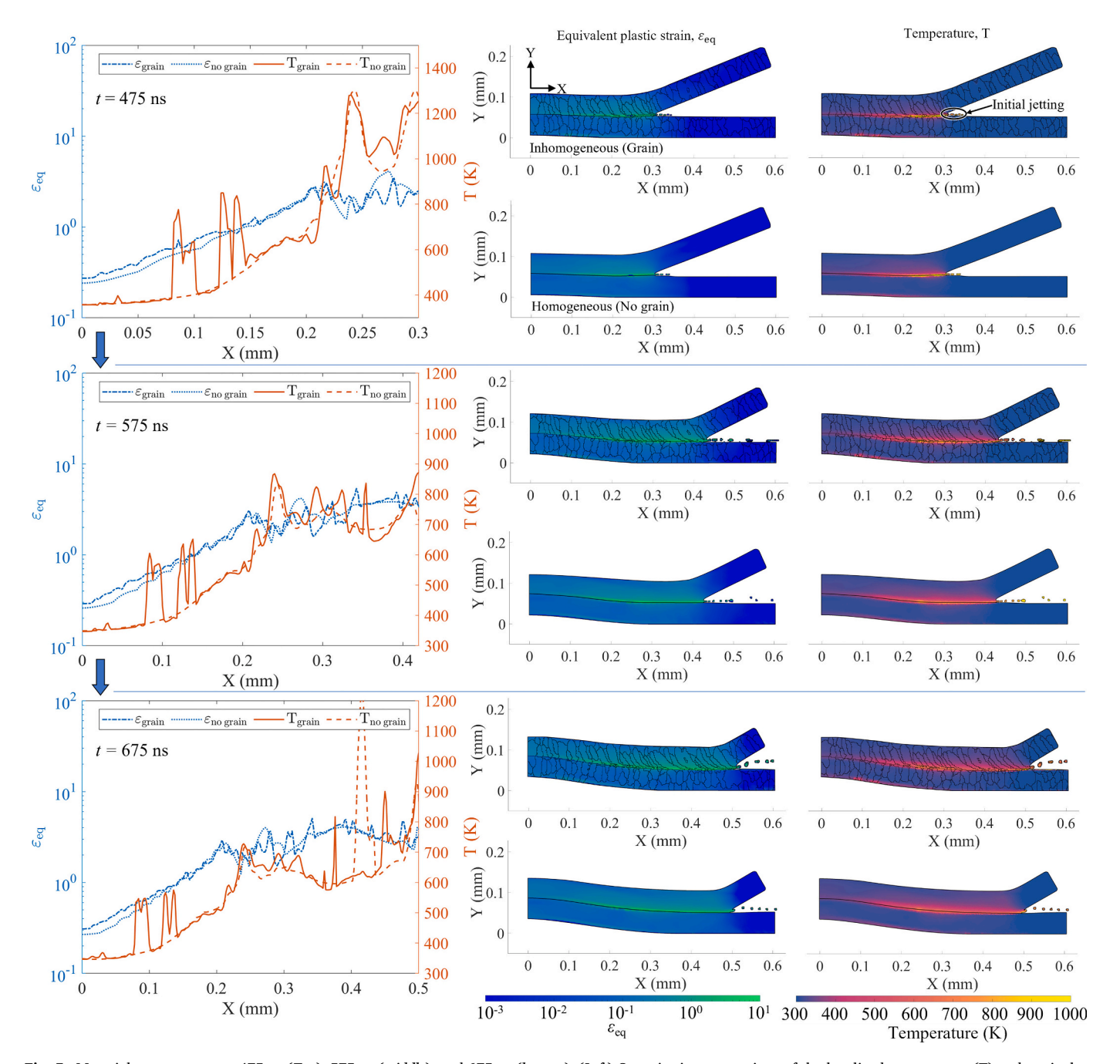


Fig. 5. Material response at t = 475 ns (*Top*), 575 ns (*middle*), and 675 ns (*bottom*). (*Left*) Quantitative comparison of the localized temperature (T) and equivalent plastic strain ( $\varepsilon_{eq}$ ) sampled along the contact interface in both inhomogeneous (grain) and homogeneous (no grain) models. (*Right*) Qualitative comparison of distribution of equivalent plastic strain ( $\varepsilon_{eq}$ ) and temperature (T) for inhomogeneous and homogeneous models. (For interpretation of the reference to color in the figure, the reader is referred to the online version of this article.)

within the respective foils, as driven by variations in yield surfaces among individual grains, gives rise to relatively higher collision velocity,  $v_x$ , of 1540 m s<sup>-1</sup>, contrasted with the homogeneous model's 1420 m s<sup>-1</sup>. The consequent increase in plastic strain rates at the interface, along with greater amounts of plastic heat dissipation, offers an explanation for the increased volume of ejecta at higher jet temperatures. (2) Variations in flow stress also promote intergranular shear instabilities that spur more fluctuations (or peaks) in equivalent plastic strain  $\varepsilon_{\rm eq}$ , as seen in the corresponding plot. Accordingly, there are also more localized peaks in temperature T predicted along the collision interface. Given the extreme temperatures that have been observed at metallic material interfaces in impact welding experiments [57] and the unstable, concentrated stresses at impact welding collision points, significant variations in temperatures are likely to present at the interface. With the inclusion of an equation of state, the effects of varying deformation among grains of varying hardness are seen in the increased occurrence of thermal spikes among the inhomogeneous temperature data (Fig. 5 left).

Near the end of the joining process (t = 675 ns, ref. Fig. 5 bottom) peak values of  $\varepsilon_{eq}$  exceed 1 in a region approximately 10 µm thick at the interface, with this threshold surpassed in both the flyer and target materials in both cases. The inhomogeneous model shows the elongation of Al grains at the emerging interface, and  $\varepsilon_{\rm eq}$  values reach 5.06 in the grained flyer. More notable, however, is the peak value of 3.96 that appears in the grained SS target at the weld, where the local reference yield strength, A, is 327.8 MPa (ref. Eq. (16)), which is among the highest 10% for this material property in the inhomogeneous model. The severe plastic deformation may result in a partial martensitic phase transformation of the SS 304 material within this distance from the interface, with the shear bands acting as new nucleation sites [58]. When examining the thermal profiles, an extreme peak T of 1261 K occurs in the homogeneous model at X = 0.42 mm, while the inhomogeneous model reaches 1027 K at the weld front (X=0.5 mm). The thermal peak of the homogeneous model is coincident with an extreme compressive stress, and without the modeling of the latent heat of fusion, the equation of state predicts a temperature spike that reflects what is most likely to be a negligible localized melt region. The inhomogeneous model's temperature peak is coincident with the stilladvancing collision point, where the plastic dissipation is still the dominant thermal effect responsible for the elevated temperatures throughout the weld region (0.15 < X < 0.5 mm).

While the presented framework does not directly capture DRX, the

propensity for grain refinement is suggested along the 10  $\mu$ m thick band near the weld interface (X > 0.15 mm) where  $\varepsilon_{eq}$  > 1 for the aluminum flyer. At the interface, a peak  $\varepsilon_{eq}$  of 5.06 is predicted, far exceeding the refinement threshold; and during processes involving severe plastic deformation, fine equiaxed grains ranging from 0.1 to 1  $\mu$ m in diameter have been observed to arise in aluminum [59], along with an associated increase in the alloy's hardness [60]. However, the occurrence of DRX cannot be confirmed, due to the very short timeframe of the LIW process (<1  $\mu$ s).

During the early stages of jet formation shown in Fig. 6, a pronounced concentration of shear stress is found in the target foil, with peak values of 634 MPa and 733 MPa at the weld front (X  $\sim$  0.3 mm) for the homogeneous and inhomogeneous models at t=475 ns, respectively. Given the significantly higher yield strengths and elastic moduli of stainless steel versus aluminum in both cases, greater magnitudes for both maximum and minimum shear stresses are expected due to the elastic response. However, the -555 MPa minimum found in the inhomogeneous target is located in the rebound region at X  $\sim$  0.1 mm, whereas the homogeneous target's -399 MPa minimum is found trailing the weld front in the shear wake (X  $\sim$  0.175 mm), consistent with the homogeneous model in a previous work [7]. Finally, shear stress minima return to the shear wake loci immediately trailing the weld front at (X, t) = (0.375 mm, 575 ns) and (0.45 mm, 675 ns) in both models.

## 4. Conclusions

The computational framework presented investigates changes in transient phenomena such as temperature, equivalent plastic strain, and shear stress during a laser impact welding process involving two dissimilar metal foils. The influence of microstructure modeling on the anisotropic material response during collision of the foils is also examined and reveals the following key findings:

- The imposition of a variable flow stress according to a J-C H-P model causes temperatures to be intermittently further elevated along the weld interface due to concentrations of shock pressure at relatively small grains.
- Grain boundary sliding, driven by variations in yield surfaces among individual grains, gives rise to relatively higher collision velocity during the weld. Consequently, higher plastic strain rates along with

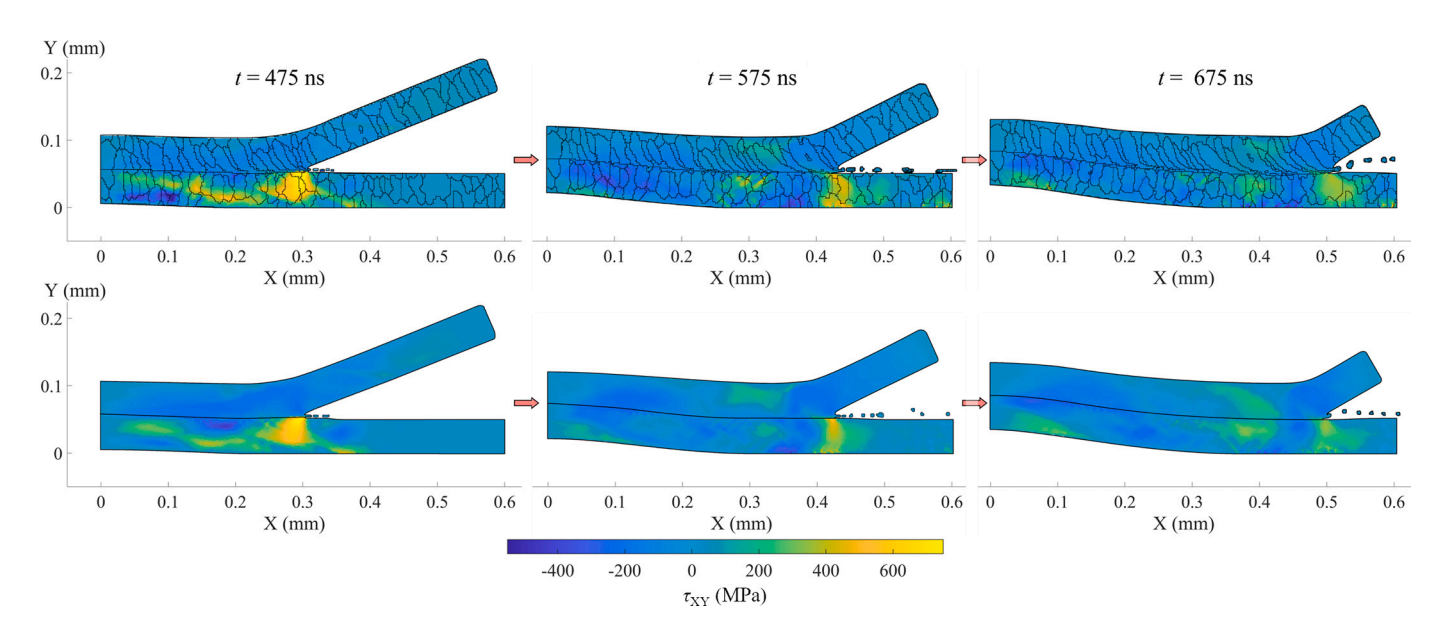


**Fig. 6.** Distribution of shear stress,  $\tau_{XY}$ , at t = 475 ns (*left*), 575 ns (*center*), and 675 ns (*right*), for the inhomogeneous (grain) model (*top*) and the homogeneous (no grain) model (*bottom*).

- greater amounts of plastic heat dissipation at the interface result in increased material jetting that occurs at higher jet temperatures.
- The patterns of alternating shear stresses emerging during weld formation vary not just in terms of their peak values according to whether grained structures are modeled, but also in terms of distribution—with a significant difference found in the magnitude of shear stress in the rebound region that persists only for a short time, indicating transient internal stress concentrations in the target that are not indicated in the homogeneous model.
- Severe plastic deformation occurs in a narrow region at the interface, suggesting grain refinement, material hardening, and phase change; however, the differences in the plastic deformation are less pronounced than those of temperature and shear stress. Moreover, the variation of flow stresses in the inhomogeneous model is not deemed to be a significant source of instability to initiate or otherwise affect the formation of the joint.

# Declaration of competing interest

The authors declare that they have no known competing financial interests or personal relationships that could have appeared to influence the work reported in this paper.

# Acknowledgements

The authors acknowledge support in part from the U.S. National Science Foundation, grant no. CMMI-1762722. Any opinions, findings, or conclusions expressed in this paper are those of the authors and do not necessarily reflect the views of the U.S. National Science Foundation.

#### References

- Wang X, Li F, Huang T, Wang X, Liu H. Experimental and numerical study on the laser shock welding of aluminum to stainless steel. Opt Lasers Eng 2019;115: 74–85
- [2] Sunny S, Gleason G, Mathews R, Malik A. Simulation of laser impact welding for dissimilar additively manufactured foils considering influence of inhomogeneous microstructure. Mater Des 2021;198:109372.
- [3] Xiong L, Cheng J, Chuang AC, Hu X, Sun X, Singh D. Synchrotron experiment and simulation studies of magnesium-steel interface manufactured by impact welding. Mater Sci Eng A 2021;813:141023.
- [4] Gao H, Ye C, Cheng GJ. Deformation behaviors and critical parameters in microscale laser dynamic forming, 2009.
- [5] Groche P, Becker M, Pabst C. Process window acquisition for impact welding processes. Mater Des 2017;118:286–93.
- [6] Sadeh S, Malik A. Investigation into the effects of laser shock peening as a post treatment to laser impact welding. Mater Des 2021;205:109701.
- [7] Gleason G, Sunny S, Sadeh S, Yu H, Malik A. Eulerian modeling of plasma-pressure driven laser impact weld processes. Procedia Manuf 2020;48:204–14.
- [8] Wang X, Tang H, Shao M, Jin H, Liu H. Laser impact welding: investigation on microstructure and mechanical properties of molybdenum-copper welding joint. Int J Refract Met Hard Mater 2019;80:1–10.
- [9] Sadeh S, Gleason GH, Hatamleh MI, Sunny SF, Yu H, Malik AS, Qian D. Simulation and experimental comparison of laser impact welding with a plasma pressure model. Metals 2019;9(11):1196.
- [10] Nassiri A, Zhang S, Lee T, Abke T, Vivek A, Kinsey B, Daehn G. Numerical investigation of CP-Ti & Cu110 impact welding using smoothed particle hydrodynamics and arbitrary Lagrangian-Eulerian methods. J Manuf Process 2017; 28:558–64.
- [11] Zhang ZL, Feng DL, Liu MB. Investigation of explosive welding through whole process modeling using a density adaptive SPH method. J Manuf Process 2018;35: 169–89.
- [12] Gupta V, Lee T, Vivek A, Choi KS, Mao Y, Sun X, Daehn G. A robust processstructure model for predicting the joint interface structure in impact welding. J Mater Process Technol 2019;264:107–18.
- [13] Lee T, Nassiri A, Dittrich T, Vivek A, Daehn G. Microstructure development in impact welding of a model system. Scr Mater 2020;178:203–6.
- [14] Liang H, Luo N, Shen T, Sun X, Fan X, Cao Y. Experimental and numerical simulation study of Zr-based BMG/Al composites manufactured by underwater explosive welding. J Mater Res Technol 2020;9(2):1539–48.
- [15] Meng Z, Gong M, Guo W, Liu W, Huang S, Hua L. Numerical simulation of the joining interface of dissimilar metals in vaporizing foil actuator welding: Forming mechanism and factors. J Manuf Process 2020;60:654–65.
- [16] Hosseinzadeh S, Mostofi TM, Babaei H. Impact spot welding of Al/Cu dissimilar metals using gas mixture detonation technique: An experimental investigation and finite element simulation. J Manuf Process 2021;65:455–70.

- [17] Li JS, Sapanathan T, Raoelison RN, Hou YL, Simar A, Rachik M. On the complete interface development of Al/Cu magnetic pulse welding via experimental characterizations and multiphysics numerical simulations. J Mater Process Technol 2021;296:117185.
- [18] Li Z, Wang X, Yang H, Ni P, Li F, Liu H. Numerical studies on laser impact welding: smooth particle hydrodynamics (SPH), Eulerian, and SPH-Lagrange. J Manuf Process 2021;68:43–56.
- [19] Lu J, Liu H, Wang K, Zhang H, Gu X, Wang X. Experimental and numerical investigations on the interface characteristics of laser impact-welded Ti/brass joints. J Mater Eng Perform 2021;30(2):1245–58.
- [20] Wang X, Shao M, Gao S, Gau JT, Tang H, Jin H, Liu H. Numerical simulation of laser impact spot welding. J Manuf Process 2018;35:396–406.
- [21] Gleason G, Sunny S, Mathews R, Malik A. Numerical investigation of the transient interfacial material behavior during laser impact welding. Scr Mater 2022;208: 114325.
- [22] Nassiri A, Kinsey B, Chini G. Shear instability of plastically-deforming metals in high-velocity impact welding. J Mech Phys Solids 2016;95:351–73.
- [23] Hung CH, Sutton A, Li Y, Shen Y, Tsai HL, Leu MC. Enhanced mechanical properties for 304L stainless steel parts fabricated by laser-foil-printing additive manufacturing. J Manuf Process 2019;45:438–46.
- [24] Sunny S, Yu H, Mathews R, Malik A, Li W. Improved grain structure prediction in metal additive manufacturing using a dynamic kinetic Monte Carlo framework. Addit Manuf 2021;37:101649.
- [25] Heigel JC, Lane BM. Measurement of the melt pool length during single scan tracks in a commercial laser powder bed fusion process. J Manuf Sci Eng 2018;140(5).
- [26] Goldak J, Chakravarti A, Bibby M. A new finite element model for welding heat sources. Metall Trans B 1984;15(2):299–305.
- [27] Sunny S, Gleason G, Bailey K, Mathews R, Malik A. Importance of microstructure modeling for additively manufactured metal post-process simulations. Int J Eng Sci 2021;166:103515.
- [28] Isbell WM, Shipman FH, Jones AH. Hugoniot equation of state measurements for eleven materials to five megabars. In: General Motors Technical Center Warren MI Materials and Structures Lab; 1968.
- [29] Handbook AM. Properties of wrought aluminum and aluminum alloys. In: ASM International Hand Book Committee. 2; 1990. p. 62–122.
- [30] Kim CS. Thermophysical Properties of Stainless Steels (No. ANL-75-55). Ill.(USA): Argonne National Lab; 1975.
- [31] Rodgers TM, Madison JD, Tikare V. Simulation of metal additive manufacturing microstructures using kinetic Monte Carlo. Comput Mater Sci 2017;135:78–89.
- [32] Plimpton S, Thompson A, Slepoy A. Stochastic Parallel Particle Kinetic Simulator (No. SPPARKS). Albuquerque, NM (United States): Sandia National Lab.(SNL-NM); 2008.
- [33] Williams CL. Structure-property relationships under extreme dynamic environments: shock recovery experiments. In: Synthesis SEM lectures on experimental mechanics. 2(1); 2019. p. 1–155.
- [34] Hung CH, Li Y, Sutton A, Chen WT, Gong X, Pan H, Leu MC. Aluminum parts fabricated by laser-foil-printing additive manufacturing: processing, microstructure, and mechanical properties. Materials 2020;13(2):414.
- [35] Mertens A, Delahaye J, Dedry O, Vertruyen B, Tchuindjang JT, Habraken AM. Microstructure and properties of SLM AlSi10Mg: understanding the influence of the local thermal history. Procedia Manuf 2020;47:1089–95.
- [36] Wen CD. Experimental investigation of emissivity of aluminum alloys and application of multispectral radiation thermometry. In: International Heat Transfer Conference, 49408; 2010. p. 867–75.
- [37] Lee T, Zhang S, Vivek A, Daehn G, Kinsey B. Wave formation in impact welding: study of the Cu–Ti system. CIRP Ann 2019;68(1):261–4.
- [38] Rusin NM, Skorentsev AL, Kolubaev EA. Dry friction of pure aluminum against steel. J Frict Wear 2016;37(1):86–93.
- [39] Raoelison RN, Sapanathan T, Buiron N, Rachik M. Magnetic pulse welding of Al/Al and Al/Cu metal pairs: consequences of the dissimilar combination on the interfacial behavior during the welding process. J Manuf Process 2015;20:112–27.
- [40] Hatamleh MI, Mahadevan J, Malik A, Qian D, Kovacevic R. Prediction of residual stress random fields for selective laser melted A357 aluminum alloy subjected to laser shock peening. J Manuf Sci Eng 2019;141(10).
- [41] Fabbro R, Fournier J, Ballard P, Devaux D, Virmont J. Physical study of laser-produced plasma in confined geometry. J Appl Phys 1990;68(2):775–84.
- [42] Hong X, Wang S, Guo D, Wu H, Wang J, Dai Y, Xie Y. Confining medium and absorptive overlay: their effects on a laser-induced shock wave. Opt. Lasers Eng. 1998;29(6):447–55.
- [43] Hall EO. The deformation and ageing of mild steel: III discussion of results. Proc Phys Soc London, Sect B 1951;64(9):747.
- [44] Petch NJ. The fracture of metals. Prog Met Phys 1954;5:1-52.
- [45] Johnson GR, Cook WH. Fracture characteristics of three metals subjected to various strains, strain rates, temperatures and pressures. Eng Fract Mech 1985;21(1): 31-48
- [46] Armstrong RW. Engineering science aspects of the Hall-Petch relation. Acta Mech 2014;225(4):1013–28.
- [47] Robinson JL. The mechanics of wave formation in impact welding. Philos Mag 1975;31(3):587–97.
- [48] Menikoff R. Empirical equations of state for solids. In: ShockWave Science and Technology Reference Library. Berlin, Heidelberg: Springer; 2007. p. 143–88.
- [49] Schino AD, Salvatori I, Kenny JM. Effects of martensite formation and austenite reversion on grain refining of AISI 304 stainless steel. J Mater Sci 2002;37(21): 4561–5.

- [50] Kamikawa N, Huang X, Tsuji N, Hansen N. Strengthening mechanisms in nanostructured high-purity aluminium deformed to high strain and annealed. Acta Mater 2009;57(14):4198–208.
- [51] Harrison W, Loupias C, Outrebon P, Turland D. Experimental data and hydrocode calculations for hypervelocity impacts of stainless steel into aluminium in the 2–8 km/s range. Int J Impact Eng 1995;17(1–3):363–74.
- [52] Liu BC, Palazotto A, Vivek A, Daehn GS. Impact welding of ultra-high-strength stainless steel in wrought vs. additively manufactured forms. Int J Adv Manuf Technol 2019;104(9):4593–604.
- [53] Dodd B, Bai Y. Adiabatic Shear Localization: Frontiers and Advances. Elsevier; 2012.
- [54] Tang L, Chen Z, Zhan C, Yang X, Liu C, Cai H. Microstructural evolution in adiabatic shear bands of copper at high strain rates: electron backscatter diffraction characterization. Mater Charact 2012;64:21–6.
- [55] Boakye-Yiadom S, Bassim N. Microstructural evolution of adiabatic shear bands in pure copper during impact at high strain rates. Mater Sci Eng A 2018;711:182–94.

- [56] Astafurov SV, Maier GG, Melnikov EV, Moskvina VA, Panchenko MY, Astafurova EG. The strain-rate dependence of the Hall-Petch effect in two austenitic stainless steels with different stacking fault energies. Mater Sci Eng A 2019;756:365–72.
- [57] Bellmann J, Lueg-Althoff J, Niessen B, Böhme M, Schumacher E, Beyer E, Böhm S. Particle ejection by jetting and related effects in impact welding processes. Metals 2020;10(8):1108.
- [58] Choi JY, Jin W. Strain induced martensite formation and its effect on strain hardening behavior in the cold drawn 304 austenitic stainless steels. Scr Mater 1997;36(1):99–104.
- [59] Horita Z, Fujinami T, Nemoto M, Langdon TG. Equal-channel angular pressing of commercial aluminum alloys: grain refinement, thermal stability and tensile properties. Metall Mater Trans A 2000;31(3):691–701.
- [60] Ito Y, Edalati K, Horita Z. High-pressure torsion of aluminum with ultrahigh purity (99.9999%) and occurrence of inverse Hall-Petch relationship. Mater Sci Eng A 2017;679:428–34.